Imager that combines near-infrared diffusive light and ultrasound

Q. Zhu

Department of Electrical and Systems Engineering, University of Connecticut, Storrs, Connecticut 06269

T. Durduran, V. Ntziachristos, M. Holboke, and A. G. Yodh

Department of Physics and Astronomy and Department of Bioengineering, University of Pennsylvania, Philadelphia, Pennsylvania 19104

Received April 5, 1999

We introduce an imaging technique that combines complementary features of ultrasound and near-infrared diffusive light imaging. We achieve the combined technology experimentally by mounting an ultrasound array together with multiple laser source and optical detector fibers upon a hand-held probe. The technique is demonstrated with tissue phantoms wherein both acoustic and optical sensors image the volume underneath the probe. Coregistration of acoustic and optical images is achieved with an accuracy of 0.27 ± 0.20 cm, approximately half of the image pixel size of our prototype. Accurate determination of target optical absorption is also achieved by use of image segmentation on the ultrasound reconstruction. The combined technique may provide improved breast-cancer detection sensitivity and specificity. © 1999 Optical Society of America

OCIS codes: 170.5280, 170.3830, 170.3010, 170.3660, 170.7170.

Ultrasound is a well-developed medical diagnostic that is used extensively for differentiation of cysts from solid lesions in breast examinations, and it is routinely used in conjunction with mammography. Ultrasound can detect breast lesions that are a few millimeters in size[1]; however, its specificity in breast-cancer detection is not high as a result of the overlapping characteristics of benign and malignant lesions.[2] Recently another modality, optical diagnostics based on diffuse near-infrared (NIR) light, has been employed in breast-cancer detection.[3–7] Functional imaging with NIR light has the potential to differentiate tumors from normal breast tissue through determination of tissue parameters such as blood volume, blood O_2 saturation, tissue light scattering, water concentration, and the concentration and lifetime of exogenous contrast agents. Current instruments can distinguish simple structures approximately 1 cm in size, but sharp edges are typically blurred by a few millimeters.[8] Thus, whereas the optical method offers new routes to tumor specificity, the relatively low resolution of the optical reconstructions makes it difficult to take full advantage of this contrast.

In this Letter we demonstrate the feasibility of a novel imaging instrument that combines ultrasound and NIR optics; the combined approach has been suggested as a potentially better means to detect heterogeneities inside tissue.[9,10] We establish a workable deployment of an ultrasound array and optical sensors such that both imaging sensors view the same geometry of the breast or other organ, and we determine the coregistration accuracy of the ultrasound and optical images for such configurations. Inasmuch as sound and light have different contrast mechanisms and propagation paths, it is not *a priori* obvious how the target will be located within ultrasound and optical images. The experiment represents what is to our knowledge the first simultaneous deployment of ultrasound and NIR sensors and demonstrates that coregistration can be achieved. Furthermore, our measurements show how segmentation of the ultrasound image can be used to improve the accuracy of optical property estimation of the target. We note that our approach differs from that used recently in the photoacoustic community in which sound is used to tag light signals.[11,12]

The probe consists of a planar surface (Fig. 1) that accommodates multiple optical sources and detectors mounted around a two-dimensional ultrasound crystal array. The planar device can in principle be used in reflection mode for breast imaging with light, ultrasound, or both. We use the device to image a tissue phantom, in which the coordinate z denotes depth into the sample from the surface and the $x-y$ plane is parallel to the probe plane. The ultrasound array is made from 20 small piezoelectric crystals located at the center of the combined probe with the crystals distributed in a rectangular 2 cm × 1.6 cm matrix. The two-dimensional (2-D) ultrasound array provides spatial $x-y$ images of the medium at various depths (z) below the surface. Such $x-y$ images can

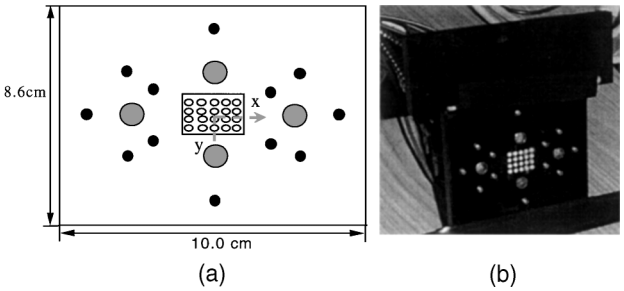

Fig. 1. (a) Sketch and (b) photograph of the combined probe (front view). An ultrasound array made from 20 crystals in a rectangular 2 cm × 1.6 cm grid is located at the center of the probe. An optical array made from 12 source fibers (smaller, darker filled circles) and 4 APD light detector fibers (larger, lighter filled circles) is located at the periphery of the probe. The coordinate axes are shown in (a).

0146-9592/99/151050-03$15.00/0

be coregistered with optical images. Note that such 2-D ultrasound arrays are not commercially available, although fabrication of such arrays is possible in research labs and by companies. The optical system consists of twelve light sources derived from a single diode laser and four detector fibers coupled to four avalanche photodiodes (APD's).

Each ultrasound piezoelectric crystal works in pulse-echo mode (i.e., it transmits and receives ultrasound pulses). The central frequency of the crystal is 5 MHz, and the bandwidth is ~50%. This type of frequency and bandwidth is used in diagnostic breast imaging. The diameter of the crystal is 1.5 mm (KS6-5-X, Ultra Lab, Inc.). The crystals are unfocused, so their angular responses are wide. The wide angular response permits formation of coherent beams from a group of transducers or a subarray. The crystals are spaced by 4 mm in both x and y directions. This spacing represents a compromise between optimum field of view and resolution. Figure 2 is a block diagram of the ultrasound data-acquisition system. During data acquisition the pulser generates a 1-cycle rf pulse with a 120-V peak that drives one crystal at a time selected by a 20:1 high-voltage multiplexer board (Matrix Corporation). The multiplexer is controlled by a PC through its serial port. The rf signals that return are received one crystal at a time, amplified by the preamplifiers (AD604, Analog Devices), and switched by a COMS 20:1 multiplexer board. The selected channel is amplified by the second-stage amplifier and sampled by a high-speed analog-to-digital conversion (A/D) board (Gage Applied, Inc.) at a sampling rate of 40 MHz. Measurements obtained from all transmission and reception positions are weighted to form the focused coherent beam output. The focal depth is ~30 mm, which is approximately the target position in our experiments. A total of 20 beams steered straight ahead were formed, and no beam steering was used in image formation because of the sparse nature of the array. Therefore the field of view is restricted to the area covered by the transducers (2 cm × 1.6 cm). We form a 2-D $x-y$ image slice by detecting the envelope signals of the coherent beams within a time window and summing the envelope signals within the window. We obtain a sequence of 2-D $x-y$ image slices by dividing the total propagation depth into consecutive time windows. The slice thickness used in the experiments varies from 2 to 5 mm in depth.

The NIR imaging instrument used in this study is based on an existing frequency-domain instrument described in Ref. 13. The intensity of the laser diode is modulated at ~200 MHz. We use two wavelengths in these experiments, 776 and 834 nm.

The diffusive wave NIR light imaging is based on the propagation and scattering of diffuse photon density waves. Measurements made at the multiple source–detector positions can be used in various image reconstruction schemes to determine the absorption and scattering coefficients of the tissue volume at slice depths below the probe. In the present experiments we use perturbation theory within the Rytov approximation to generate a set of coupled linear equations that relate the measured optical signals to absorption and scattering variations in each volume element within the sample. We then employ the algebraic reconstruction technique to solve these equations iteratively. However, for the reconstructions presented in this Letter we did not attempt to determine absorption and scattering simultaneously; instead we reconstructed absorption alone or scattering alone. This procedure was thus susceptible to cross coupling of absorption and scattering, so we do not expect to determine the true optical properties in samples that contain both scattering and absorption heterogeneities. The reconstruction scheme yields an image of the optical properties of the three-dimensional sample volume (8.0 cm × 6.4 cm × 4.0 cm) beneath the probe surface. The reconstructed voxels measured 1.0 cm × 1.0 cm × 1.0 cm, so the number of unknowns and the number of measured parameters were kept approximately the same; the images were virtually unchanged in reconstruction, with voxels of size 0.4 cm × 0.4 cm × 1.0 cm. Therefore we reconstructed 0.4 cm × 0.4 cm × 1.0 cm voxels for with ultrasound images.

We also reconstructed optical properties from a segmented image determined by the ultrasound. For this calculation we used a Rytov iterative method based on finite-difference forward calculations and a regularized conjugate gradient method for the inversion.[14] In this scheme we used the ultrasound image to determine heterogeneity and background voxels, thereby reducing the number of unknown optical properties to four. The numerical calculation yielded properties that were accurate for optical absorption but less accurate for optical scattering.

Figure 3 shows an example of coregistered optical absorption (left) and ultrasound (right) images obtained from the combined probe. The optical wavelength used was 776 nm. The target was a 1.2-cm-diameter resin sphere 2.6 cm deep in an Intralipid solution. The size of the image pixel was 0.4 cm × 0.4 cm in both ultrasound and optical images. The physical size of the ultrasound image was 2 cm by 1.6 cm, and the image was geometrically centered with the optical image. A slice of the optical image is shown at a depth $z = 2.5$ cm into the medium, and we obtained the ultrasound image by summing the envelope signals from 2.2 to 2.7 cm. Thus the ultrasound image shows the integrated reflectivity of a 0.5-cm-thick slice.

The background optical absorption coefficient was $\mu_a = 0.04\ \text{cm}^{-1}$, and the reduced scattering coefficient was $\mu_s = 3.5\ \text{cm}^{-1}$. The target μ_a and μ_s', 0.2 and 12 cm^{-1}, respectively, were intended to simulate tumor

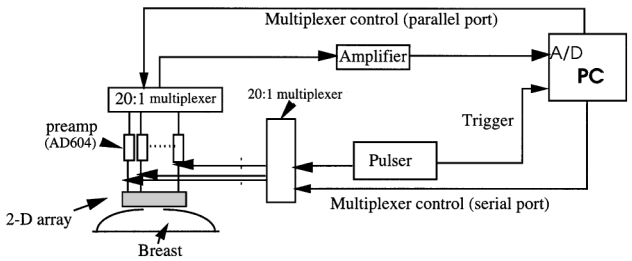

Fig. 2. Electronic configuration of the ultrasound data-acquisition system.

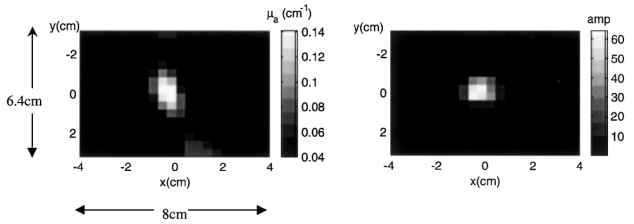

Fig. 3. Optical absorption (left) and ultrasound (right) images of the same target embedded inside an Intralipid solution.

optical properties. The algebraic reconstruction technique solution based on the Rytov perturbative approximation was able to reconstruct a stable location and size of the target in μ_a and μ_s' images in approximately 20,000 iterations. As expected, the optical properties were not accurate, though the positional information was always good. We were, however, able to reconstruct the optical properties of the heterogeneity more accurately by using the segmentation method. This method has a stopping criterion based on the minimum error between the measured and the computed optical signals. The minimum expected error was determined from numerical computations with the actual optical properties. The method was then started from homogeneous background optical properties and iterated until the error approached the minimum expected error. The optical properties found were $\mu_a = 0.203\ \mathrm{cm}^{-1}$ and $\mu_s' = 7.58\ \mathrm{cm}^{-1}$. μ_s' was not so accurately determined. This inaccuracy may be related to the relatively large errors in measuring the phase of detected signals that are typical of these measurements[15] and is especially important when there are relatively few source–detector pairs.

The acoustic reflectivity of the resin sphere was moderate, and the image is thus scaled from 0 to 64 gray levels. The target reflectivity can be estimated from its reflection coefficient (R). R between the resin sphere and Intralipid is ~0.2, whereas R in human body tissue ranges from 0.01 (soft tissue) to 0.5 (bony tissue structure). Thus the target acoustic contrast to background liquid is within the physiological contrast range.

To measure the coregistration accuracy we chose the spatial distance between the peaks of ultrasound and corresponding optical images as a criterion. To determine the peak locations more accurately we used weighted bicubic interpolation to interpolate the images to an 8-times-finer pixel size. For example, after interpolation, the peak of the ultrasound image shown in Fig. 3 is located at ($x = -0.175$ cm, $y = 0.075$ cm), and the peak of the μ_a image is located at ($x = -0.185$ cm, $y = 0.075$ cm). The calculated coregistration error is 0.01 cm. Six samples with different μ_a and μ_s' at two wavelengths were studied. The measured average coregistration error in image location is 0.27 ± 0.20 cm. Thus coregistration is achieved with an accuracy of about half of the pixel size.

In conclusion, a prototype 2-D combined imager has been constructed. The imager provides spatially coregistered ultrasound and NIR diffusive light images. Experiments indicate that imaging of the tissue volume underneath the combined probe is feasible, and adequate coregistration of optical and acoustic images can be achieved. The combined imaging technique illustrates a new way to utilize the advantages of ultrasound and NIR imaging techniques to improve cancer diagnosis. Further improvement of the prototype is readily possible with more piezoelectric crystal transducers and with commercial 2-D ultrasound arrays when they become available. The optical reconstruction is readily improved with more source–detector pairs and better imaging algorithms.

The authors thank Robert Danen for assistance with the NIR imager and Britton Chance and Bernard Steinberg for valuable comments. In addition, we thank Don Carlson, Marc Rosenstock, Anil Patel, and Dafina Steward for help with data collection and instrumentation. Q. Zhu acknowledges partial support from the U.S. Army (DAMD-17-94-J-4133) and research foundations of University of Pennsylvania and the University of Connecticut. A. G. Yodh acknowledges partial support from the U.S. Army (DAMD17-97-1-7272) and the National Institutes of Health (CA75124-01). Q. Zhu's e-mail address is zhu@engr.uconn.edu.

References

1. T. A. Stavros, D. Thickman, and C. Rapp, Radiology **196,** 123 (1995).
2. B. B. Goldberg, J. B. Liu, and F. Forsberg, Ultrasound Med. Biol. **20,** 319 (1994).
3. M. A. Franceschini, K. T. Moesta, S. Fantini, G. Gaida, E. Gratton, H. Jess, M. Seeber, P. M. Schlag, and M. Kashke, Proc. Natl. Acad. Sci. USA **94,** 6468 (1997).
4. J. B. Fishkin, O. Coquoz, E. R. Anderson, M. Brenner, and B. J. Tromberg, Appl. Opt. **36,** 10 (1997).
5. T. L. Troy, D. L. Page, and E. M. Sevick-Muraca, J. Biomed. Opt. **1,** 342 (1996).
6. R. J. Grable, D. P. Rohler, and S. Kla, Proc. SPIE **2979,** 197 (1997).
7. B. Chance, S. Nioka, S. Zhou, and E. Conant, "Simple, fast, breast-tumor hypoxia imager," Proc. SPIE **3597** (to be published).
8. A. Yodh and B. Chance, Phys. Today **48**(3), 34 (1995).
9. Q. Zhu, D. Sullivan, B. Chance, and T. Dambro, IEEE Trans. Ultrason. Ferroelectr. Freq. Control **46,** 665 (1999).
10. B. J. Tromberg, University of California, Irvine, Irvine, Calif. 92612 (personal communication, 1999).
11. L. Wang, S. L. Steven, and X. Zhao, Opt. Lett. **20,** 629 (1995); L. Wang and G. Ku, Opt. Lett. **23,** 975 (1998).
12. S. Leveque, A. C. Boccara, M. Lebec, and H. Saint-Jalmes, Opt. Lett. **24,** 181 (1999).
13. R. M. Danen, Y. Wang, X. D. Li, W. S. Thayer, and A. G. Yodh, Photochem. Photobiol. **67,** 33 (1998).
14. Y. Yao, Y. Wang, Y. Pei, W. Zhu, and R. L. Barbour, J. Opt. Soc. Am. A **14,** 325 (1997).
15. N. Ramanujam, C. Du, H. Y. Ma, and B. Chance, Rev. Sci. Instrum. **69,** 3042 (1998).